

Evolution of a block cave from time-lapse passive source body-wave traveltime tomography

Jean-Philippe Mercier¹, Willem de Beer¹, Jean-Pascal Mercier², and Simon Morris³

ABSTRACT

Most underground mines are equipped with microseismic monitoring systems that allow the detection, location, and characterization of microseismic events. Microseismic events can be exploited to understand the rock mass response to mining. However, seismicity provides information only for regions that are seismically active. Although some information on nonseismically active regions can be obtained from point measurements and numerical modeling, these methods suffer from limitations of their own. Passive source traveltimes body-wave tomography (passive source tomography [PST]) uses information readily collected by microseismic monitoring systems, namely, the P- and/or S-wave traveltimes and microseismic event hypocenter locations. This technique allows the simultaneous estimation of the velocity distribution between sensors and microseismic events and the correction of microseismic event hypocenter locations. In this paper, we present an application of time-lapse

PST to the Northparkes Mines E26 Lift 2 block cave showing that PST can be used to obtain information on evolution and distribution of seismic velocities, leading to a better understanding of stress distribution and redistribution and of rock mass behavior during the development and production phases. In particular, we found that (1) the magnitude of the velocity perturbation varied through time and appeared to be strongly correlated with the intensity of microseismic activity, the mining rate, and the nature of the mining activity, (2) the velocity models provided information that allowed for the inference of the cave geometry and its evolution through time, (3) the stress distributions inferred from the velocity model were not fully consistent with a widely accepted conceptual stress redistribution model, which may reflect the significant influence of rock mass inhomogeneities and the mining sequence, (4) seismicity was found in regions in which velocity was higher and lower than the background velocity, and (5) there was no obvious correlation between geology and velocity distribution and evolution.

INTRODUCTION

Induced microseismicity provides reliable information on rock mass response to human activities such as mining, hydrocarbon reservoir treatments (e.g., hydrofracturing) and depletion, and surface reservoir impoundments. Nowadays, many underground mines are equipped with modern microseismic monitoring systems that provide 3D coverage of the rock mass. These microseismic monitoring systems allow the location of microseismic event hypocenters, often to within 5 m, and the characterization of the microseismic activity through the calculation of a series of source parameters (e.g., moment magnitude, radiated seismic energy). The microseismic data

can be exploited to monitor the time evolution and spatial variation of microseismic activity (e.g., [Gibowicz et al., 1994](#); [Mendecki, 1996](#)) and gain a better understanding of the rock mass behavior in response to mining activity, albeit only in areas of a mine in which seismic activity occurs.

To obtain information on rock mass behavior in areas that are not seismically active, geotechnical engineers typically rely on point measurements (e.g., in situ stress and deformation measurements) and/or numerical modeling. The locations of point stress and displacement measurements provide localized information and are constrained by logistical and access considerations. Numerical modeling of rock mass behavior is based on simplified assumptions,

Manuscript received by the Editor 3 April 2014; revised manuscript received 12 August 2014; published online 9 February 2015.

¹Golder Associates Ltd., Montreal, Quebec, Canada. E-mail: jpmmercier@golder.com; wdebeer@golder.com.

²Advanced GeoScience Imaging Solutions Ltd., Montreal, Quebec, Canada. E-mail: jpmmercier@gmail.com.

³Golder Associates (NZ) Ltd., Dunedin, New Zealand. E-mail: smorris@golder.com.

© 2015 Society of Exploration Geophysicists. All rights reserved.

uses limited information on rock mass structure and geology, and is sensitive to boundary conditions. Numerical modeling consequently provides results that are difficult to verify and that may diverge considerably from the true rock mass response. This is especially valid in the case of block caving operations, in which access to the caving orebody is limited and the rock mass failure process and subsequent flow of broken material are complex phenomena that are not yet fully understood.

Passive source body-wave traveltimes seismic tomography (passive source tomography [PST]) is a geophysical inversion method that can be used to estimate the rock mass response in regions (not necessarily seismically active) located between seismic sensors and microseismic events. In block caving operations, PST does not suffer from limited access to the caving orebody, nor does it require any knowledge of the physics of the caving process or rock mass properties, structure, or geology. PST exploits the P- and/or S-wave arrival time measurements readily available from recorded and processed microseismic events to compute the distribution of P- and/or S-wave velocities in the monitored volume of rock and correct for microseismic event hypocenter locations.

The velocity models calculated using PST can be used to assess the spatiotemporal distribution of stress and fractures in the rock mass and perform time-lapse imaging. There is empirical evidence of the relation between seismic velocity and stress (e.g., Wyllie et al., 1958; Christensen and Wang, 1985; Prasad and Manghnani, 1997; Hofmann et al., 2005; Silver et al., 2007; Niu et al., 2008) as well as theoretical justifications (e.g., Nur and Byerlee, 1971; Gangi and Carlson, 1996; Gurevich, 2004). It is also becoming clear that seismic tomography, including PST, can image the spatial distribution and temporal variation of mining-induced stress (Young and Maxwell, 1992; Maxwell and Young, 1996; de Beer et al., 2012; Westman, 2012). Unless other factors enter into play, the higher the stress, the higher the P- and S-wave velocities. In the context of mining, seismic velocities higher than the background or average seismic velocities are usually observed in regions in which stress concentrates. By contrast, low velocities are observed in regions in which stresses are shed.

In this paper, we present 24 P-wave time-lapse velocity models calculated using PST from microseismic data collected from January 2004 to December 2004 at the Northparkes Mines (NPM) E26 Lift 2 block caving mine. Our velocity models cover the last part of the undercut and the draw phases, up to breakthrough into Lift 1 directly above. Our results show temporal variations of the spatial stress distribution in an area that consistently encompasses a large portion of the orebody for all the velocity models. The PST results presented in this paper provide important clues to the distribution and evolution of stress in the E26 Lift 2 cave and may have potentially allowed the detection and remediation of uneven stress distribution, had the tomography model been calculated at the time of mining.

Note that we use the words “caving” and “cave” as generic terms that refer to the damaged region above the undercut and extraction levels. This region may be a void and/or a muck pile or may consist of an in situ “plug” of fractured rock. The term plug is used here to include a plug failure, but also more generally to include the notion of a region of failed rock that may transition gradually into the host rock or abutments. The term “anomaly” will be used to denote a (positive or negative) deviation from the average, or background homogeneous velocity, determined using calibration blasts.

CONTEXT

Block caving

Brown (2007) gives a fairly concise introduction to the block caving method. Here, we summarize the salient points. Block caving is a so-called mass mining method in which an equi-(three) dimensional block of ore is undercut to induce the rock above to collapse. The undercut zone is developed by drilling and blasting, and some ore is drawn off to create a void for the overlying ore to collapse into. A production or extraction level is constructed below the undercut level and connected to it by drawbells through which broken rock flows as it is removed from drawpoints on the extraction level. In theory, the progressive removal of broken rock causes the void (cave) to grow upward, through the orebody or block, in principle through to surface, in which subsidence then occurs.

In practice, this propagation of a cave is dependent on several factors, among them the “caveability” of the ore. This could depend on the rock type (kimberlite pipes are often amenable to caving, for example) or the degree of jointing and “blockiness” of harder rock types. Other factors include the in situ stress regime and the draw sequence. More often than not, in hard rock environments, the caving process requires preconditioning through blasting or hydrofracturing to maintain and control progression of the cave.

Northparkes Mines (NPM): E26 Lift 2

The E26 Lift 2 mine is part of the NPM. This copper and gold mine is located approximately 27 km from the town of Parkes in the central-west region of New South Wales, Australia, and it is currently composed of four economic deposits named Endeavour 22, 26, 27, and 48, typically referred to as E22, E26, E27, and E48. Exploration in the area started in the 1970s, and open cut (open pit) mining of the E22 and E27 deposits started in 1993. Underground development of E26 Lift 1 also started in 1993, and production followed three years later. E26 Lift 1 aimed to exploit the orebody from surface to a depth of 480 m below surface. It was the first block caving mine in Australia and ranked for a few years as the most productive hard rock underground mining operation in the world (Lye et al., 2006). E26 Lift 2, the mine of interest in this study, was designed to exploit the orebody from the base of E26 Lift 1 to a depth of 830 m below surface. The size of the E26 Lift 2 extraction level is approximately $200 \times 160 \text{ m}^2$. Development of E26 Lift 2 started in 2002, and the mine was commissioned in late 2004.

Geology and in situ premining stresses

The ore reserves at NPM are mainly located in copper/gold-bearing porphyries (see Figure 1), deposited during the Late Ordovician (460–450 Ma) in the Goonumbra Volcanic Complex. Mineralization is typically located in narrow, pipelike quartz monzonite porphyry (QMP) intrusive complexes. E26 Lift 2 is composed of four major geologic units: the QMP, the volcanics, the Biotite quartz monzonite (BQM), and the diorite. The QMP represents the orebody and is composed of a series of subvertical fingers and veins. The volcanics date from the late Ordovician era and are mostly located on the west side of the orebody. The BQM, another volcanic unit, is mostly located on the east side of the orebody. Finally, the diorite intersects the orebody between Lift 1 and Lift 2 from the west (a more comprehensive review of the NPM geology is presented in Lickfold et al., 2003). As shown in Table 1, rock strength

varies slightly from one geologic unit to another, the BQM being the strongest and the volcanics the weakest (Chen, 1996).

In situ premining stress conditions at NPM were measured using CSIRO hollow inclusion cells at a depth of 813 m. The details of the measurements are discussed in an internal report (ITASCA, 2005, Northparkes mines, Technical Report); the results are presented in Table 2. The stress measurements indicate that the principal stress σ_1 is 53 MPa in magnitude, subhorizontal, and oriented roughly east–south. The magnitudes of the σ_2 and σ_3 components are 33 and 22 MPa, respectively. The intermediate stress component σ_2 is approximately horizontal and oriented north–south, whereas σ_3 is nearly vertical.

Mining sequence

The E26 Lift 2 extraction level is located approximately 830 m below the surface and 350 m below the E26 Lift 1 extraction level. Development of E26 Lift 2 adopted a preundercut approach that can be considered a variant of the advance undercut approach (see Brady, 2004, p. 472). This method is used to minimize the risk of drawbell damage posed by the high induced-stress concentration related to undercutting in the abutment ahead of the undercut front. In this approach, the development of the undercut leads to the development of the extraction horizon.

The development of the E26 Lift 2 undercut started in late February 2003. The development of the undercut and extraction levels started from the southwestern corner of the E26 Lift 2 footprint and progressed roughly northeasterly. The undercut was finalized in January 2004, and the extraction level was completed in August 2004. Production started shortly thereafter, and the E26 Lift 2 cave broke through E26 Lift 1 in December 2004. The caving at E26 Lift 2 was rapid and irregular, and a wedge of uncaved material formed in the top southwest corner of the E26 Lift 2 block.

Microseismic monitoring system

The microseismic activity at E26 Lift 2 was monitored by an array composed of 19 triaxial accelerometers and nine uniaxial geophones (White et al., 2004) (see Figure 2). The sensors were deployed relatively close to the orebody in a 3D geometry designed to ensure accurate detection and location of microseismic events throughout the caving process and to mitigate the shadowing effect expected from the growing cave. In 2004, the microseismic monitoring system was sensitive to microseismic events down to a moment magnitude of -2.0 as reported by Hudyma et al. (2007a, 2007b) and shown by the cumulative (tail) frequency-magnitude relationship (Gutenberg and Richter, 1965) presented in Figure 3. The average location accuracy afforded by the array is estimated by White et al. (2004) to be approximately 6 m.

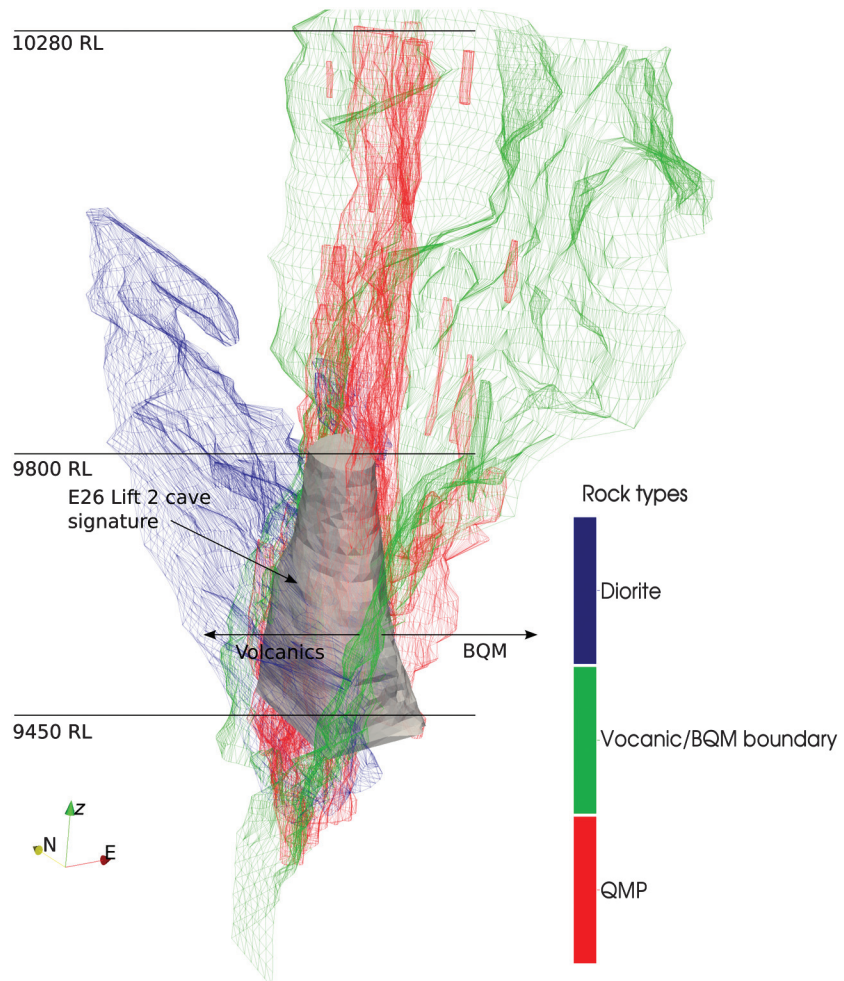


Figure 1. Oblique 3D view of the NPM E26 main geologic features. Australian mine datum is generally at 10,000 m; for instance, relative level (RL) = 10,280 m represents an elevation 280 m above mean sea level.

Table 1. Intact rock strengths in the E26 orebody at NPM (Chen, 1996).

Rock type	Uniaxial compressive strength (MPa)
Volcanics	116
QMP	124
BQM	143

Table 2. In situ premining stress conditions from measurements at NPM taken at 813-m depth (ITASCA, 2005, Northparkes mines, Technical Report).

Principal stresses component	Magnitude (MPa)	Dip (°)	Bearing (°)
σ_1	53	10	96
σ_2	33	1	186
σ_3	22	80	283

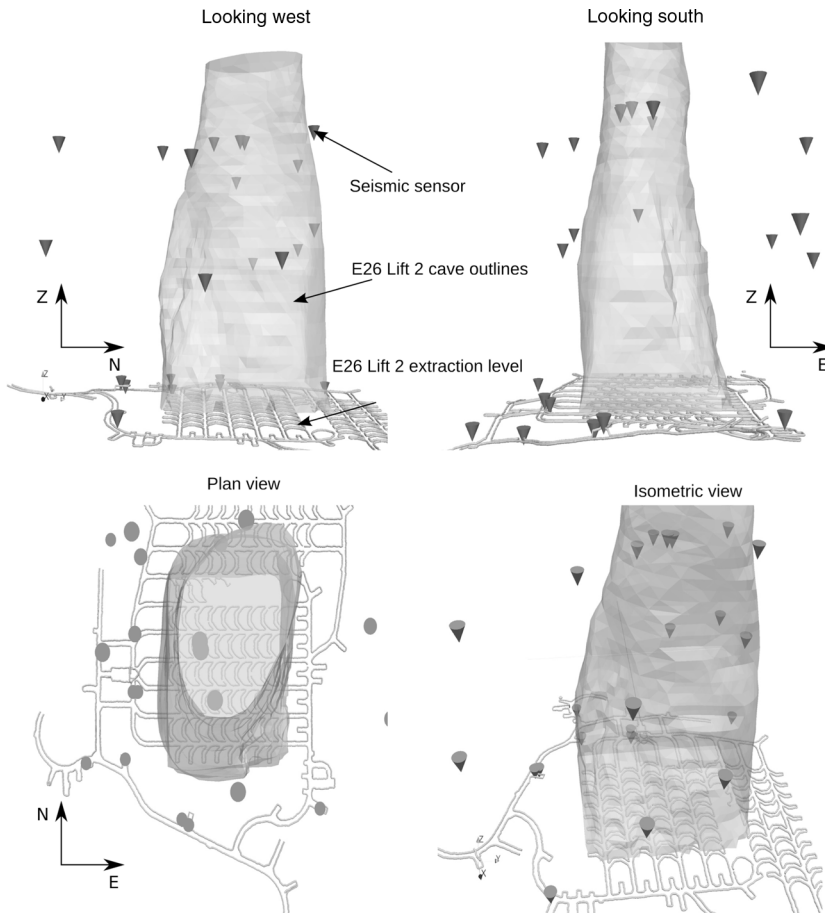


Figure 2. Location of seismic sensors with respect to the cave and E26 Lift 2 extraction level, access, and decline.

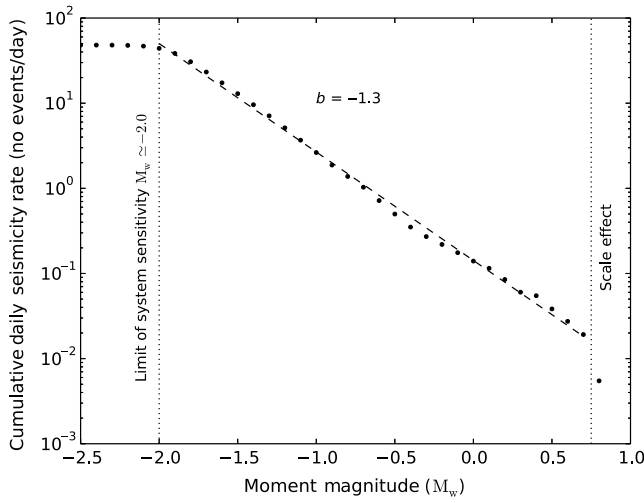


Figure 3. Frequency magnitude plot for the data set used in this study. The dashed line represents the trend line fit through the cumulative event magnitude frequency distribution for moment magnitude (M_w) of -2.0 to 1.0 , inclusively. The system sensitivity is estimated to be $M_w = -2.0$. Monitoring volume and duration scale effect are observed for events larger than M_w .

Conceptual stress distribution model and seismic velocities

The sketches in Figure 4a and 4b were adapted from Brown (2007, Figure 6.11) and show a 2D view of a conceptual stress redistribution model for a homogeneous rock mass during the undercutting and caving phases, respectively. According to this model, during the undercut process, the stress is compressional in the abutments and it is extensional directly above the undercut. During the caving process, stress in the abutments remains compressional and tends to rotate toward the vertical whereas the stress above the cave becomes compressional. From this conceptual model, considering the sensitivity of the P velocity to stress, it is expected that a seismic velocity higher than the background velocity will be observed in the abutments during the undercut and the caving process. During the caving process, higher velocities could also be expected above and around the cave in the region commonly referred to as the seismogenic zone. This so-called seismogenic zone is described by several authors (e.g., Brady, 2004; Flores, 2005; Hudyma et al., 2007a, 2007b; Westman, 2012) as the locus of the most intense seismic activity related to the caving process. Seismic velocities lower than the background velocity are expected directly above the undercut front during undercutting and within the zone of mobilized and yielded rock once the caving process starts.

METHOD

Problem definition

The relation among the arrival time T_{ij} , velocity $\mathbf{v}(\mathbf{x})$, and origin time τ_{e_i} for an event i located at \mathbf{x}_{e_i} and recorded at a sensor j located at \mathbf{x}_{s_j} is as follows:

$$T_{ij} = \int_{L(\mathbf{v}(\mathbf{x}), \mathbf{x}_{e_i}, \mathbf{x}_{s_j})} \mathbf{v}^{-1}(\mathbf{x}) dl + \tau_{e_i}, \quad (1)$$

where $\int_{L(\mathbf{v}(\mathbf{x}), \mathbf{x}_{e_i}, \mathbf{x}_{s_j})} \mathbf{v}^{-1}(\mathbf{x}) dl$ represents the traveltime t_{ij} , and $L(\mathbf{v}(\mathbf{x}), \mathbf{x}_{e_i}, \mathbf{x}_{s_j})$ is the raypath. Note that the boldface \mathbf{x} denotes a Cartesian coordinate vector and that in general boldface type denotes vectors or matrices.

The relation in equation 1 is nonlinear because the trajectory between source i and receiver j , along which the seismic energy travels, depends on the underlying velocity model $\mathbf{v}(\mathbf{x})$ and the event hypocenter location \mathbf{x}_{e_i} and because the event hypocenter location and origin time depend on the velocity model.

Inverse problem

We are interested in recovering the 3D velocity and the event hypocenter locations from measurement of arrival times. To do so, we choose to solve for the velocity model, event hypocenter locations, and event origin time adopting an iterative nonlinear

approach, alternating forward modeling (ray tracing) and linear inversion until convergence is achieved. Note that in this paper, we refer to the combination of forward modeling and linear inversion as nonlinear inversion.

At each nonlinear iteration n , the velocity, event hypocenter locations, and event origin times are updated by adding perturbations to the model parameters as follows:

$$\mathbf{x}_e^{n+1} = \mathbf{x}_e^n + \partial\mathbf{x}_e^n, \quad (2)$$

$$\mathbf{v}(\mathbf{x})^{n+1} = \mathbf{v}(\mathbf{x})^n + \partial\mathbf{v}(\mathbf{x})^n, \quad (3)$$

and

$$\boldsymbol{\tau}_e^{n+1} = \boldsymbol{\tau}_e^n + \partial\boldsymbol{\tau}_e^n. \quad (4)$$

The perturbations are calculated by solving the following linear system, which is a linearized version of equation 1:

$$\partial\mathbf{t}^n = \mathbf{F}^n \partial\mathbf{m}^n, \quad (5)$$

where $\partial\mathbf{t}^n$ is the traveltime residual vector ($\mathbf{t}_{\text{observed}} - \mathbf{t}_{\text{predicted}}$), \mathbf{F}^n is the Fréchet derivative matrix that represents the sensitivity of each traveltime with respect to the model parameters ($\partial\mathbf{T}^n / \partial\mathbf{m}^n$), and $\partial\mathbf{m}^n$ is the model perturbation vector ($\mathbf{m}^n = [\mathbf{x}_{e_1}, \dots, \mathbf{x}_{e_j}, v_1, \dots, v_k]$). The Fréchet derivative matrix is updated at each nonlinear iteration and depends mainly on the ray geometry and the velocity along the raypaths.

The inversion is regularized by imposing damping to the solution, and the linear system is solved using the conjugate gradient method, minimizing the following cost (objective) function at every iteration:

$$\min_{\mathbf{v}, \mathbf{e}} (\Phi_t + \lambda_v \Phi_v + \lambda_e \Phi_e), \quad (6)$$

where Φ_t represents the data misfit ($\|\partial\mathbf{t}^n\|_2$), λ_v and λ_e are free parameters controlling the level of damping imposed on the model parameters, Φ_v measures the difference between the updated \mathbf{v}^{n+1} and current \mathbf{v}^n velocities ($\|\mathbf{v}^{n+1}(\mathbf{x}) - \mathbf{v}^n(\mathbf{x})\|_2$), and Φ_e measures the distance between the updated \mathbf{e}^{n+1} and current \mathbf{e}^n ($\|\mathbf{e}^{n+1} - \mathbf{e}^n\|_2$).

To ensure that the velocity model obtained after each nonlinear iteration $\mathbf{v}^n(\mathbf{x})$ is smooth and continuous, we filter the 3D velocity distribution using a Gaussian moving average filter after the inversion process.

Forward modeling

Forward modeling involves solving the eikonal equation to recover the traveltimes from every source point (here, sensors s_j) at every points of the forward grid ($\mathbf{t}_{s_j}(\mathbf{x})$) and to calculate the event-sensor raypaths and the Fréchet derivatives.

The eikonal equation describes the propagation of the seismic wavefront in elastic media and is expressed as follows:

$$(\nabla_{\mathbf{x}} \mathbf{t}_{s_j}(\mathbf{x}))^2 = (\mathbf{v}^{-1}(\mathbf{x}))^2, \quad (7)$$

where $\nabla_{\mathbf{x}}$ represents the gradient in Cartesian coordinates. We solve the eikonal equation using the fast marching method (Sethian, 1999) recovering $\mathbf{t}_{s_j}(\mathbf{x})^2$ for every source points.

The raypath is constructed by following the direction of steepest descent given by the gradient of the traveltime grids. This can be accomplished by solving the following ordinary differential equation using an explicit fourth-order Runge-Kutta method:

$$L(\mathbf{v}(\mathbf{x}), \mathbf{x}_{e_i}, \mathbf{x}_{s_j}, t) = \nabla_{\mathbf{x}} \mathbf{t}_{s_j}(\mathbf{x})^2. \quad (8)$$

We calculate the Fréchet derivative by first dividing the constructed raypath into segments of equal length l . We then use cubic spline interpolation to attribute a velocity v_l to each segment as a function of the velocity of surrounding grid nodes. Finally, we take the derivative of the traveltime function, $t_{ij} = \sum_s \frac{l}{v_{ls}}$, along the raypath between event i and sensor j with respect of each model parameters.

DATA

The data set used in this study is composed of 77,500 P-wave arrival times manually picked from slightly more than 17,500 selected microseismic events recorded from the beginning of January 2004 through the end of December 2004. Figure 5 shows an example of a seismogram of a microseismic event recorded at the Northparkes E26 Lift 2 mine. The traveltimes were obtained using microseismic event hypocenter locations and origin times calculated using a probabilistic nonlinear global search location method implemented in the NonLinLoc software (Lomax et al., 2001).

The microseismic event rate varied considerably during the study period. As a consequence, the traveltimes data set is uneven. The microseismic activity in E26 Lift 2 is closely related to the undercut front advance rate and the rate of progression of the caving front,

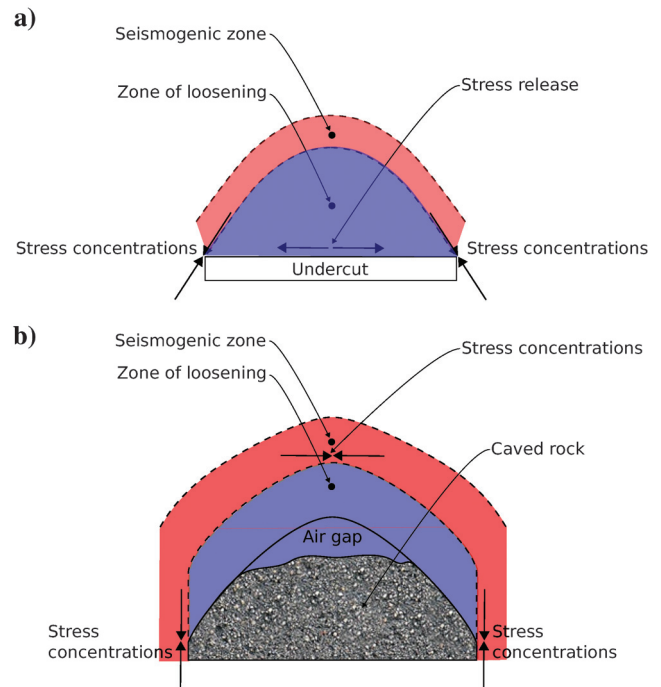


Figure 4. Conceptual stress distribution model during the caving for a homogeneous rock mass (a) during undercutting (the undercut progresses into or out of the page) and (b) during the caving process. Red and blue are used to identify regions in which the seismic velocity is expected to be higher and lower than the background velocity (adapted from Flores, 2005).

which can be closely linked to the amount of rock extracted at the draw points. Figure 6 presents the temporal distribution (by month) of the manually accepted microseismic events for 2004. During that year, the monthly averaged daily seismic activity rate varied from three events a day in April to approximately 250 events a day in October. The seismic activity can be considered high in January and from August to November and low from February to July and in December. The high seismic activity rate observed in January is associated with the end of the development of the undercut level, whereas the high activity rate in August through November is associated with caving of the rock mass.

To image the temporal variation of the seismic velocity distribution and better understand the evolution of the rock mass within the framework of the block caving process, the data set was divided into 26 subsets (24 are presented) spanning time periods varying between one week and one month, depending on the intensity of mi-

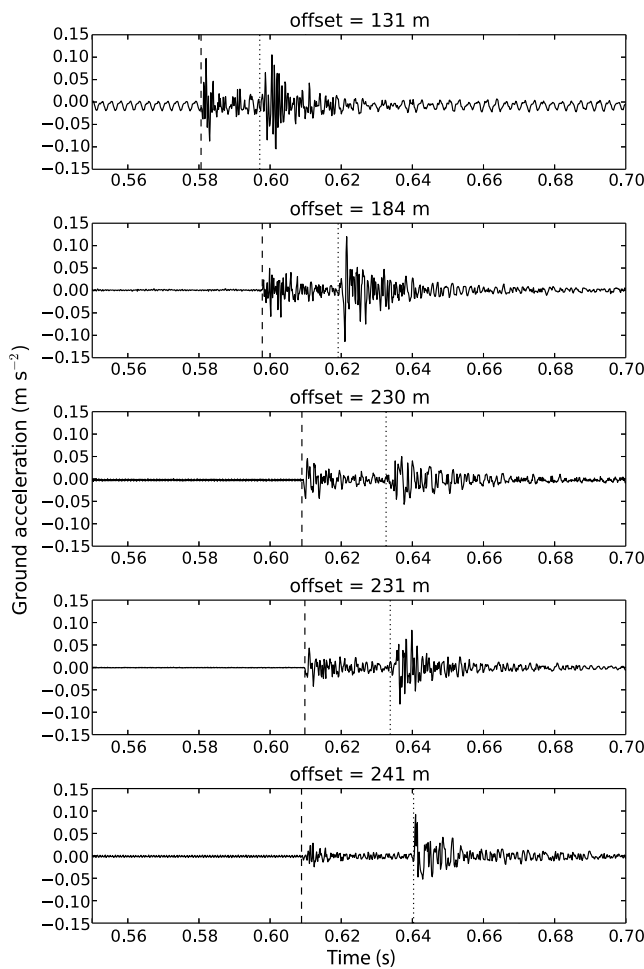


Figure 5. Unfiltered seismogram of a microseismic event of moment magnitude -1.5 recorded on 5 October 2004, at 23:00:14 (EDT Australia) by the NPM E26 mine microseismic monitoring system shown at five triaxial accelerometers. The offset represents the source-sensor distance. To better capture the P- and S-waves on a single trace, the x -, y -, and z -components were combined in a single trace in which amplitude is the square root of the sum of the amplitude of the x -, y -, and z -components multiplied by the sign of the x -component. The vertical dashed and dotted lines represent the picked P- and S-wave onset times, respectively.

croseismic activity. The period covered by each subset varies and depends on the level of microseismic activity (the January data set is a notable exception to this rule). The higher the microseismic activity, the shorter the time period covered by the velocity models. Despite this, the number of events used for each inversion may vary, but the event spatial distribution and ray coverage stay relatively similar especially in the center of the model from data set to data set. Similar ray coverage allows the comparison of velocity models calculated for different time periods.

The plot of Figure 7 shows the relation between event-sensor distance and traveltimes for all the traveltimes used in this study. The average apparent velocity (traveltimes divided by sensor-event

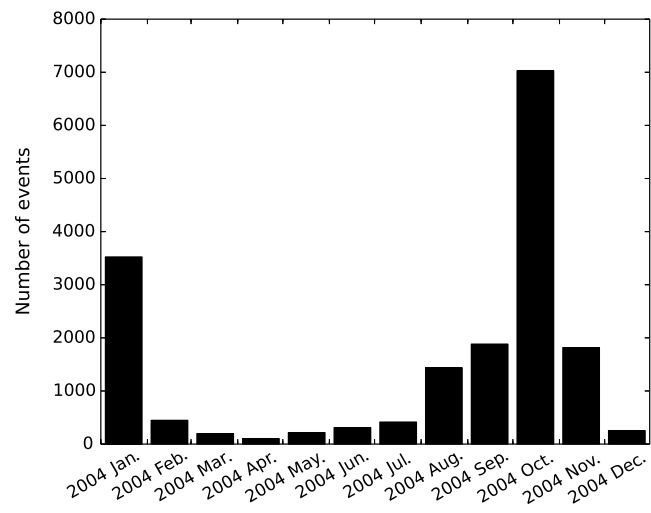


Figure 6. Time distribution of manually processed and accepted microseismic events within the volume of interest in the NPM E26 Lift 2 mine from the beginning of January 2004 to the end of December 2004.

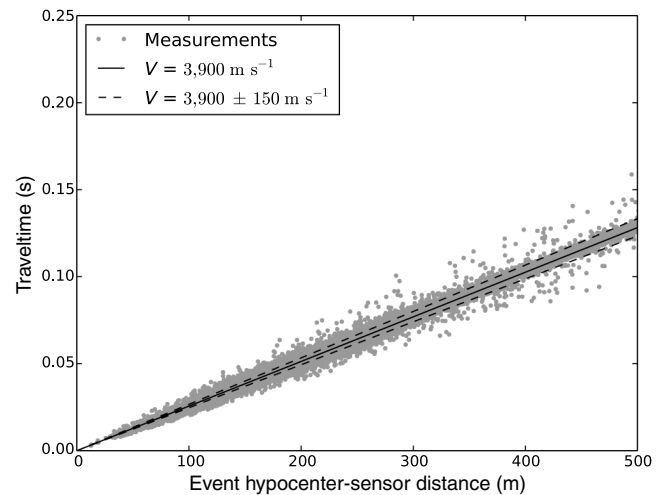


Figure 7. Traveltimes event hypocenter-sensor distance plot. The black dots represent the calculated P-wave traveltimes used to compute the P-wave velocity model obtained from the picked P-wave arrival time and event origin times. The plain and dotted red lines represent the trends along the apparent average P-wave velocity and the apparent average P-wave velocity plus/minus one standard deviation, respectively.

distance) calculated from these measurements is 3901 m s^{-1} , which is virtually the same as the calibrated velocity of 3900 m s^{-1} . The standard deviation of the apparent velocity uncertainty is around 150 m s^{-1} . Note that we did not investigate the relation between the deviation of the apparent velocity from the average velocity and the magnitude of a microseismic event. However, it is expected that, in general, the larger the magnitude of a microseismic event, the better the signal-to-noise ratio and consequently the more accurate the arrival time picks, event hypocenter location, and estimate of velocity.

INVERSION

Model parameterization

The P-wave velocity models cover a volume extending over 550 m in the north and east directions and 500 m in the z direction, thus fully encompassing the E26 Lift 2 orebody. Figures 8 presents the extent of the models. The spacing between adjacent nodes was set at 5 m in every direction, yielding a model comprising 1.21 million nodes. The velocity models are continuous; i.e., the seismic velocity is defined at the nodes, and the velocity among the nodes is interpolated by cubic splines.

Inversion procedure

All data sets were inverted following the same procedure. The starting velocity model was chosen to be homogeneous (i.e., constant), with a velocity value of 3900 m s^{-1} attributed to every node. This velocity corresponds to the average P-wave velocity obtained with calibration blasts. The inversions were performed independently on each of the models, and 20 nonlinear iterations were used. To reduce the impact of potential outliers on the output model, we only used traveltimes that resulted in residuals (the difference between the traveltime predicted using the velocity model and the observed traveltime) smaller than $1.5\sigma_{\partial t}^n$ ($\sigma_{\partial t}^n$ is the standard deviation of all of the traveltime residuals ∂t^n) for a given nonlinear iteration n . To account for the difference in the conversion rate between the event hypocenter location and velocity model (Thurber, 1992), we alternate velocity inversions and joint velocity and event hypocenter inversion during the inversion process.

As discussed previously, we regularize the inversion using damping. Regularization of an inverse problem by damping is one of the simplest forms of regularization, and its computation complexity is low compared with other types of regularization schemes that involve, for instance, the calculation of the first or second derivatives. The choice of damping levels λ_v , λ_e , and λ_{τ_0} used in the inversion has an impact on the inversion results, which vary across the model depending on the ray coverage: the better the ray coverage (rays from a variety of azimuths and elevations) and the higher the ray density, the smaller the impact of the damping levels. Too large a velocity damping factor will tend to pro-

duce flat velocity models, close to the starting velocity, that do not fit the data well, whereas too small a velocity damping factor will tend to produce a complex velocity model containing large velocity variations beyond what is required to fit the data.

To determine the appropriate level of damping to impose during the inversion, we adopted a popular approach based on the trade-off curve. This approach is described, for example, in section 2.3.2 of Rawlinson and Sambridge (2003). The trade-off curve relates the data misfit to the model complexity. The optimal trade-off between model complexities and the fit is considered to be at the point of maximum curvature also referred to as the knee of the trade-off curve. Here, we found that the optimal velocity and event hypocenter location damping levels were similar for the different data sets. Based on this, we chose to use the same damping factor of $\lambda_v = 1 \times 10^{-13}$, $\lambda_e = 1 \times 10^{-6}$, and $\lambda_{\tau_0} = 1 \times 10^{-3}$ for the inversion of all data sets. The standard deviation characterizing the Gaussian smoothing filter was set at 20 m.

Inversion quality

The ability of a tomographic velocity model to resolve localized velocity perturbations (i.e., deviations from the background) depends on the quality of the traveltimes measurements, as well as the ray distribution and ray geometry. To be well resolved, the velocity at a given node must be sampled by seismic rays coming from a variety of azimuths and incidence angles. The resolution of our velocity models was assessed by inspecting the ray distribution, ray geometry, and ray density and through the use of the checkerboard resolution test. The checkerboard resolution test uses the ray

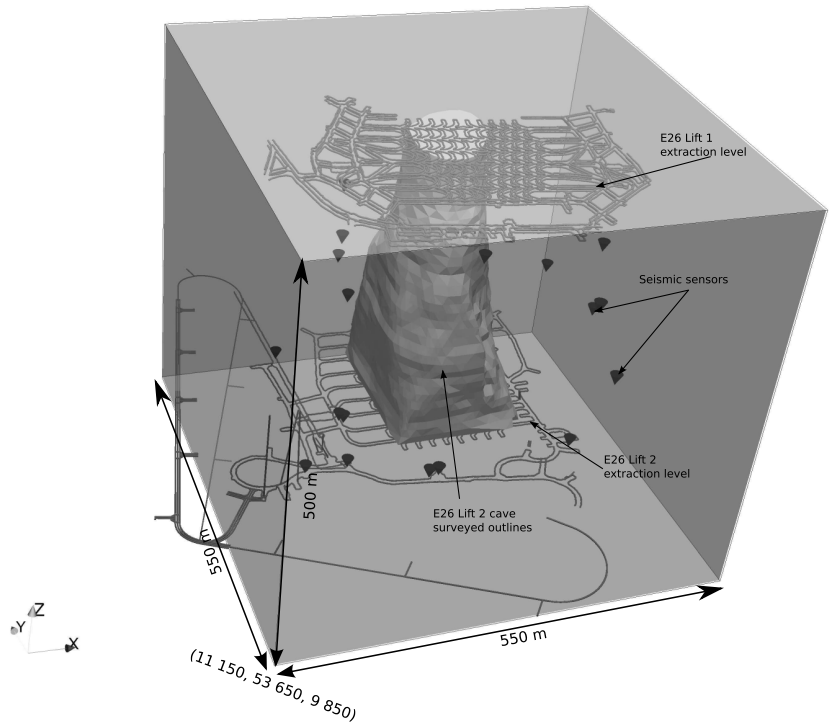


Figure 8. Extents of the velocity model. The extents of the model are represented by the gray box. Access to the E26 Lift 2 and the E26 Lift 1 and Lift 2 extraction levels are shown, as well as an outline of the cave as surveyed in 2008. The black cones represent seismic sensors.

geometry calculated at the end of the inversion process to generate a set of traveltimes using a synthetic velocity model composed of alternating high- and low-velocity perturbations. The synthetic traveltimes are then inverted, and the recovered velocity model is compared with the original checkerboard model. Many tomographic studies use this approach, in a variety of contexts, to assess inversion quality and help detect the presence of potential artifacts (Bostock and Van Decar, 1995; Zelt and Barton, 1998; Sol et al., 2002; Lebedev, 2003; Mercier et al., 2009). More information about the checkerboard resolution test can be found in Rawlinson and Sambridge (2003, section 2.4.2). Note that the known limitations of the checkerboard resolution test (Lévéque and Masson, 1999) were considered when interpreting the results.

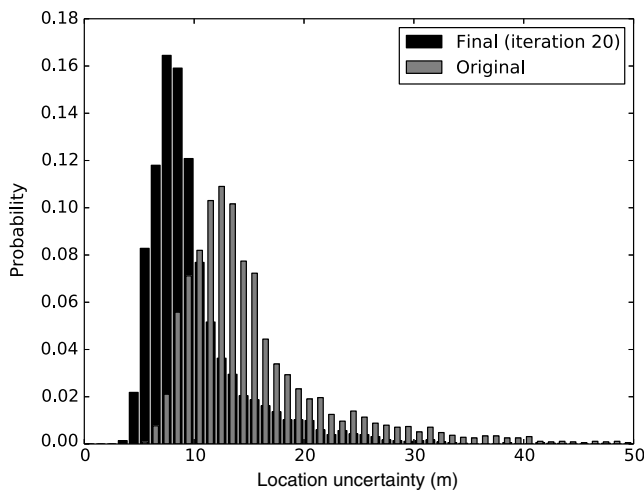


Figure 9. Distribution of event hypocenter location uncertainty at the beginning and at the end of the iteration process.

The synthetic checkerboard model created for this project is composed of alternating spherical low- and high-velocity anomalies, each 50 m in diameter. The peak velocity, which is found at the center of the perturbation, is set at 3900 ± 390 m s⁻¹, representing a deviation of about 10% from the background velocity. The magnitude of each velocity anomaly decays from the centers according to a Gaussian distribution with a standard deviation of 20 m.

RESULTS

Event location uncertainty

Figure 9 shows the event hypocenter location uncertainty distribution at the beginning and at the end of the iteration process for the January 2004 data set. The mean estimated hypocenter location uncertainty decreased from approximately 15 m at the beginning of the inversion process to 10 m after the 20th iteration. Note that the location uncertainty for each individual event was calculated by taking the square root of the maximum eigenvalue of the covariance matrix $\text{COV}(\mathbf{x}_{e_i})$. The covariance matrix is calculated as follows:

$$\text{COV}(\mathbf{x}_{e_i}) = (\mathbf{F}_{e_i}^T \mathbf{F}_{e_i})^{-1} \sigma_{\partial t}^2, \quad (9)$$

where \mathbf{F}_{e_i} represents the elements of the Fréchet derivative related to the event i and $\sigma_{\partial t}$ is the standard deviation of traveltime residual vector.

Resolution

The results of the resolution tests differ from model to model as a result of variation in ray coverage among data sets. Figure 10 presents an example of a resolution test for January 2004. Artifacts and smearing along the preferential orientations of the rays are present to varying degrees on all of the calculated velocity models.

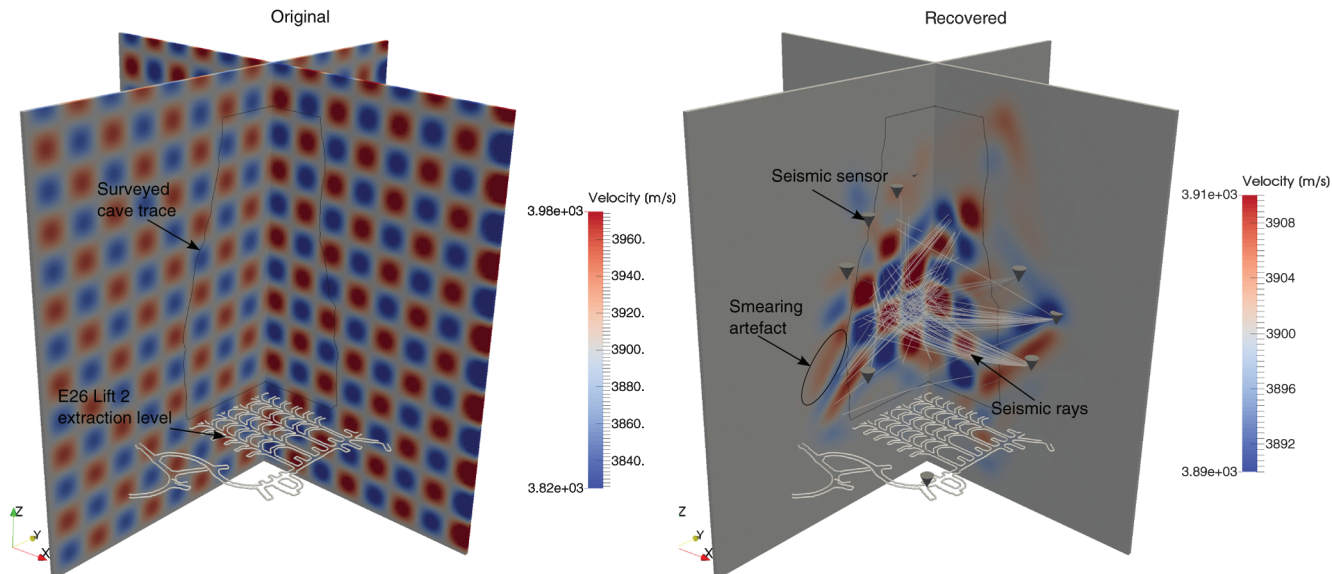


Figure 10. Orthogonal view of two cut slices through the original (left) and recovered (right) checkerboard models, using the ray geometry calculated from the January 2004 velocity model obtained after 20 nonlinear iterations. The white lines represent 1% of the raypaths calculated from the January 2004 final velocity. The cones represent the locations of seismic sensors. Smearing artifacts are observed in the periphery of the monitored volume.

Blind spots (region with poor ray coverage) exist within the E26 Lift 2 orebody. Their locations change through time. Most frequent blind spot locations within the E26 Lift 2 orebody are the lower north and upper south area. The bottom of the orebody is poorly resolved from the end of October to the end of December. The shape and location of the artifacts vary depending on the travelttime subset. Despite some differences, the results of the resolution tests share common features. (1) The resolution is best at the center of the E26 Lift 2 orebody, in which the ray density is consistently the highest and the ray geometry is the best (many rays with different azimuths and elevations crossing). In the central region, it is possible to clearly identify individual synthetic high- and low-velocity anomalies for most of the resolution test results. (2) The resolution tends to decrease outward and is nearly null at the edges of the model, in which ray coverage is poor. (3) Smearing along the preferential ray orientation is observed, mostly, but not uniquely, in peripheral regions in which the ray geometry is not optimal (i.e., in which the rays are oriented along a limited set of azimuths and elevations). In the presence of smearing, low- or high-velocity anomalies often merge to form linear features. (4) The velocity range of the recovered checkerboard model is smaller than that of the original. For instance, for the month of January, the velocity of the original checkerboard model varies from approximately 3510 to 4290 m s⁻¹, whereas the velocity of the recovered model varies from roughly 3850 to 3950 m s⁻¹.

Hypocenter corrections and velocity model statistics

Table 3 presents a series of statistics on the velocity models and event hypocenter locations calculated from the inversion results obtained after 20 nonlinear iterations. The minimum and maximum velocities observed in the models range from 2574 to 3708 m s⁻¹ and 4118 to 5127 m s⁻¹, respectively. The statistical velocity distribution obtained after 20 nonlinear iterations is nearly Gaussian for all the models, with an average velocity close to 3900 m s⁻¹ that varies approximately from 3890 to 3950 m s⁻¹. The standard deviation of the Gaussian velocity distributions varies roughly from 40 to 115 m s⁻¹. The mean and standard deviation of the event hypocenter correction varies from 3.15 to 8.20 m and from 1.11 to 6.40 m, respectively.

Velocity distribution and evolution

Figure 11 shows images of 24 of the 26 velocity models calculated from January to December 2004. As previously discussed, these velocity models span the last part of undercut development and part of the caving process up to breakthrough into E26 Lift 1. These velocity models show the temporal evolution of the P-wave velocity spatial distribution. The evolution of the velocity is gradual and does not differ radically among consecutive velocity models.

The January model is mostly dominated by a large high-velocity zone located directly above the E26 Lift 2 extraction level, extending upward over roughly 200 m, and it appears to be dipping northward. Velocity higher than background velocity is also visible in this region in the February model with a lower magnitude, however. The velocity above the E26 Lift 2 extraction level decreases again in March, and velocity lower than average is observed for most of the velocity model from April. The February model also features (1) a low-velocity zone located roughly in the middle of the Lift 2 orebody that extends upward over a few tens of meters and (2) a strong high-velocity anomaly sitting mostly at the top of the orebody that extends downward on the south side. These two features are visible as well in the March model but exhibit a slightly different character; the high velocity is more confined at the top of the orebody. From April to early November, all the velocity models are relatively similar and basically composed of two large velocity anomalies, one high and one low. For these models, the high- and low-velocity anomalies are predominantly located in the upper north and lower south regions of the E26 Lift 2 orebody, respectively. From the early November to mid-December, the high-velocity anomaly that was

Table 3. Velocity model and event hypocenter location correction statistics.

Start date	End date	P-wave velocity (m s ⁻¹)				Hypocenter location correction (m)		
		Mean	Minimum	Maximum	σ	Mean	Maximum	σ
2004-01-01	2004-02-01	3960	3853	4194	62	3.22	12.31	1.89
2004-02-01	2004-03-01	3972	3749	4311	79	2.21	8.14	1.39
2004-03-01	2004-04-01	3915	3723	4058	48	2.24	8.79	1.62
2004-04-01	2004-05-01	3879	3476	4124	86	4.38	24.05	3.88
2004-05-01	2004-06-01	3890	3530	4105	71	2.75	10.22	1.81
2004-06-01	2004-06-14	3892	3602	4049	55	2.43	6.57	1.45
2004-06-14	2004-06-28	3922	3615	4242	75	3.12	18.19	2.45
2004-06-28	2004-07-15	3929	3591	4245	68	2.23	7.15	1.44
2004-07-15	2004-07-31	3927	3797	4116	41	1.21	7.18	1.11
2004-07-31	2004-08-18	3920	3778	4188	42	2.24	7.17	1.35
2004-08-01	2004-09-08	3904	3192	4494	150	2.70	12.27	1.97
2004-08-18	2004-08-25	3920	3480	4368	93	2.26	8.50	1.56
2004-09-08	2004-09-15	3908	3529	4252	92	3.12	16.04	1.87
2004-09-15	2004-09-22	3886	3460	4272	94	2.27	9.49	1.61
2004-09-22	2004-09-29	3908	3740	4186	54	1.69	5.37	1.18
2004-09-29	2004-10-06	3850	3321	4208	124	2.55	13.11	1.79
2004-10-06	2004-10-13	3861	2931	4557	186	5.66	36.25	4.67
2004-10-13	2004-10-20	3891	3173	4510	153	5.95	38.76	5.19
2004-10-20	2004-10-27	3893	3072	4808	177	5.89	31.93	4.63
2004-10-27	2004-11-03	3926	3391	4884	148	5.42	36.66	4.36
2004-11-03	2004-11-10	3941	3493	4688	123	5.19	30.23	3.74
2004-11-10	2004-11-17	3994	3626	4545	141	7.12	37.04	5.68
2004-11-17	2004-11-24	3959	3581	5127	181	8.20	42.07	6.40
2004-11-24	2004-11-31	4037	3867	4726	135	5.61	27.01	4.16
2004-11-31	2004-12-14	4033	3742	5036	173	6.15	25.78	4.30
2004-12-14	2004-12-31	3992	3766	4217	69	3.38	11.49	2.74

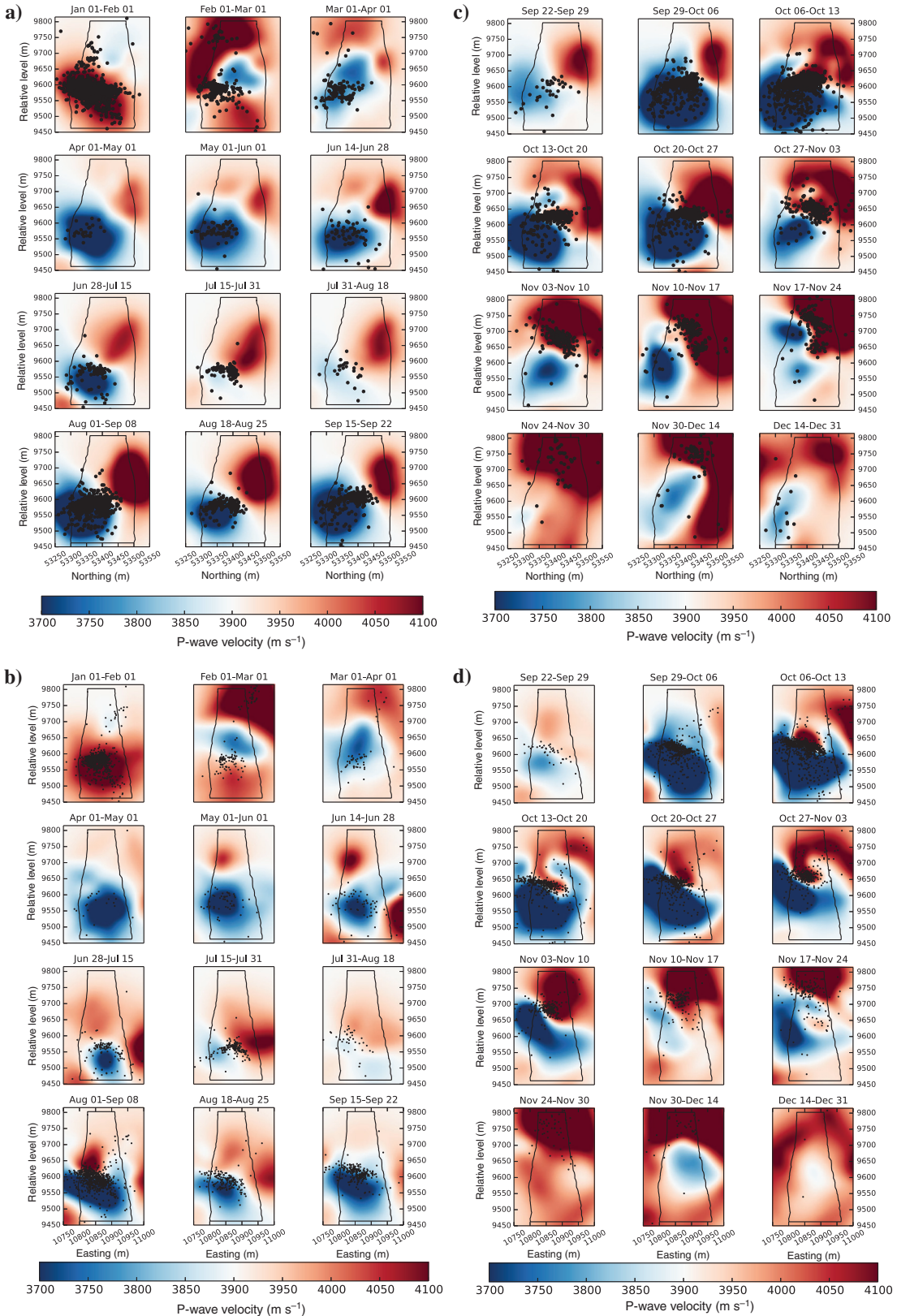


Figure 11. Cut slices through 24 (out of 26) selected velocity models calculated from January 2004 to the end of December 2004. The thick black line represents the trace of the E26 Lift 2 cave as surveyed in July 2009. The black dots represent the location of microseismic activity found within 25 m of the cut planes. In panels (a and c) is the view looking west, and in panels (b and d) is the view looking north. Red and blue represent high and low velocity, respectively. Note that the velocity is presented using the same color map and scale for all the models.

previously predominantly located at the top of the model appears to start extending downward along the sides (the models suggest mostly the north side) of the E26 Lift 2 orebody. During the same time period, our results suggest that the upper extent of the low-velocity anomaly progressed upward.

Event location and seismic velocity

In Figure 11, the locations and magnitudes of microseismic events that occurred within 25 m of the cut plane through the P-wave velocity models are represented by dots. The locations of microseismic events with respect to the high and low P-wave velocity anomalies vary throughout the study period. Microseismic activity is generally found within zones in which the velocity is higher than 3900 m s^{-1} in January and February and from the early October to mid-December and within regions of velocity lower than 3900 m s^{-1} from March to mid-July and from early August to early October.

DISCUSSION

Result quality

Ray coverage and geometry remained relatively consistent in the central region of the model, in which the effect of the caving process is expected to be dominant. The checkerboard resolution test results suggest that the resolution afforded by the data set is sufficient to see large-scale spatial variations (approximately 50 m and more) in P-wave velocity distribution within most of the E26 Lift 2 orebody for all the velocity models. Shadow zones appear within the E26 Lift 2 orebody for some models, however. The lower north portion of the E26 Lift 2 block is particularly problematic. Given the array geometry, the ray coverage highly depends on the presence of seismic activity north of this region. Smearing of the recovered velocity along the preferential ray orientation is observed but typically is localized mostly in the periphery of the models and most of the time outside of the zone of interest.

Velocity range

The range of the P-wave velocity models we have calculated is similar to the range of P-wave velocity reported by Westman (2012) for other PST study conducted in the context of block caving. Also, the standard deviation of the velocity models, which varies from 41 to 186 m s^{-1} , compares well with the value of 150 m s^{-1} calculated using raw traveltimes measurements. From the checkerboard resolution test results, it follows, however, that calculated velocity variations are potentially underestimated in some sections of the velocity models. Smearing of the velocity anomalies along raypaths is the main mechanism limiting the range of velocities (decrease in seismic activity rates often correlates with the increase in smearing). Changes in the rock P-wave velocity during the period covered by each model could be the source of inconsistencies in arrival time measurement and also contribute to limiting the range of velocity variations.

Seismic velocity and stress

We consider that stress (including stress shadowing due to fracturing) and the presence of the cave are the main factors influencing the velocity distribution and evolution of the P-wave velocity in the case of interest in this study. Seasonal surface variations (temperature or rainfall) are unlikely to have a significant influence on the

velocity at depths between 480 and 830 m where the E26 Lift 2 mine is located. An increase in pore pressure and water content is not impossible, however, but would directly relate to the level of fracturing induced by the cave progression.

It is generally accepted that a relationship exists between seismic velocity and the stress state of the rock mass. In a homogeneous rock mass, high velocities would typically be associated with regions of elevated stress, whereas low velocities would be associated with regions of lower stress. The lower stress regime could be related to damage, stress shadowing, or stress cycling.

Several authors (e.g., Yamamura, 2003; Silver et al., 2007; Niu et al., 2008) report that sensitivity of the body wave velocity to stress varies from approximately 10^{-7} to 10^{-6}Pa^{-1} . This means, for instance, that a stress variation of 10 MPa, which should not be uncommon in block cave mines, would yield deviation from the background velocity ranging from 1% to 10%, respectively (e.g., a background velocity of 4000 m s^{-1} will yield a velocity deviation of between 40 and 400 m s^{-1}).

The standard deviation σ of the recovered velocity model represents a deviation from the background velocity that varies from approximately 1% to 5% (see Table 3). We can consequently say that approximately 95% of the velocity nodes are attributed a velocity that deviates from the background or average velocity from 2% to 10% (2σ). Assuming that sensitivity to stress at E26 Lift 2 is similar to values reported in the literature, the calculated velocity at 95% of the velocity model nodes would represent variation in the magnitude stress from the in situ stress state ranging from 2 to 8 MPa or from 20 to 80 MPa for sensitivities of 10^{-6} and 10^{-7}Pa^{-1} , respectively. These values represent measurable stress change. The value obtained using a velocity sensitivity to stress of 10^{-7}Pa^{-1} appears large, although not unphysical, suggesting that the velocity sensitivity to stress in E26 Lift 2 may be closer to 10^{-6}Pa^{-1} than to 10^{-7}Pa^{-1} .

Velocity, mining, and microseismic activity

There exists a clear relation among the magnitude of the calculated velocity anomalies, mining, and the rate of microseismic activity. The magnitudes of the velocity anomalies are larger in January 2004 (end of the undercutting) and in February 2004 (possibly a long-term stress relaxation effect related to the cessation of undercut blasting) and from August to mid-December 2004, when production and cave propagation were underway. The magnitudes of the velocity anomalies are lower from March to August 2004, during the period of seismic quiescence corresponding to the final stage of development of the extraction level. The seismic activity rate correlates well with the calculated velocity range. Generally, the higher the activity rate, the higher the velocity range. In the region of the model in which ray coverage is variable, a decrease in the magnitude of the calculated velocity anomalies can be attributed to poorer ray coverage. Changes in the resolution and magnitude of the low-velocity anomaly visible at the bottom of the model from roughly March to December 2004 is a notable example of the effect of changing ray coverage on velocity. Note that the ray coverage remains relatively constant in the center of the model throughout the study period and variations in the magnitude of the calculated velocity are likely related to mining.

Cave signature

The velocity model presented in this study may allow identification of the signature of the cave and approximate tracking of the

temporal evolution of the cave geometry. As discussed in the Introduction section, we define a cave as air and broken and yielded rock, and its seismic velocity is expected to be significantly lower than the velocity of the premining *in situ* rock mass. Most of the velocity models feature a large low-velocity anomaly extending upward from the E26 Lift 2 undercut level to a height that increases with time. We interpret this feature as being the tomographic signature of the E26 Lift 2 cave.

The ability of the tomographic inversion to resolve the low-velocity anomaly that we believe is likely to be associated with the cave varies from one time period to another. It depends mostly on the density and uniformity of ray coverage afforded by each data set. Given the ray geometry and checkerboard resolution test results, the cave geometry should be relatively well resolved from January 2004 to early November 2004 despite the presence of a shadow zone localized in the bottom north area of the E26 Lift 2 orebody. This is confirmed by the presence in the velocity models of a well-defined low-velocity anomaly near the bottom of the model and the sharp contrast between low and high velocities. From November 2004 to December 2004, when ray coverage at the bottom of the model was suboptimal, the low-velocity anomaly is weaker and the contrast between low and high velocity is more diffuse.

At the time of conducting this study, we did not have access to any geotechnical data providing information on the location of the caving front (e.g., open hole measurements). We were consequently unable to compare our tomography results with other sets of observations and confirm or infirm our interpretation.

Comparison with the conceptual stress redistribution model

Our results are not fully consistent with the stress redistribution model presented earlier. From this model, we would expect to find a high-velocity zone in a relatively confined dome-shaped region above a low-velocity zone during the undercut and caving process. Our results suggest instead that the region of high velocity is not confined within a small seismogenic zone. The difference between the stress distribution suggested by the velocity model and that predicted by the conceptual model may be a reflection of the inhomogeneous composition of the E26 orebody, the intricacies of the draw sequences, or a combination of these.

Seismicity and velocity

There is a school of thought (Brown, 2007) that holds that seismic activity during the caving process would be mostly confined to the so-called seismogenic zone. This is a zone of presumed high stress (and hence high seismic velocity) above the back of the forming cave during the development of the undercut and during the caving process. Our results show that, in the case of the E26 Lift 2, there was a variable correlation between the locations of the microseismic event hypocenters and the locations of high P-wave velocity anomalies. We found that throughout the study period, a significant fraction of the microseismic activity, which includes large events, was located in regions of low P-wave velocity. If we accept that seismic velocity can be used as a reliable proxy for stress, our results mean that microseismic activity is not solely confined within the zone or region of high stresses, but it can also be found in regions in which stresses are lower than the undisturbed *in situ* stresses. In other words, high seismic activity in itself may not

imply a highly stressed area. Note that we found no significant difference among the distribution of key calculated source parameters (P- and S-wave energy ratio, moment magnitude, and static stress drop) for microseismic events found in regions of velocity higher and lower than the background velocity.

Correlation between velocity and geology

No obvious correlation was observed between the velocity models and geologic features. This may be related to the fact that the physical properties of the different rock types in the four geologic units represented in the E26 Lift 2 mine are very similar and that they can all be classified as very strong rock. This suggests that in this case, P-wave velocity is mainly influenced by the distribution of stresses in the rock mass, and not the geology.

Velocity and caving behavior

The PST time-lapse results show that the seismic velocity distribution is asymmetrical. High seismic velocity predominantly tends toward the southwest, in January, February, and to some extent March, and then to the northeast. The asymmetrical velocity distribution might be related to the uneven geometry of the final E26 Lift 2 cave. Had PST velocity modeling been conducted at the time of the undercut development and during the caving process, it may have allowed early detection of anomalous rock mass behavior and mitigation of conditions that yielded uneven cave geometry.

CONCLUSION

In this study, we presented 24 P-wave velocity models using P-wave traveltimes data from the NPM E26 Lift 2 covering a time period extending from early January to late December 2004. The velocity models cover the last portion of the undercut and extraction level developments and part of the production phase. The velocity models were calculated by adopting an approach that alternated linear tomographic inversion and ray tracing in a series of nonlinear iterations.

The time-lapse tomographic results can be considered to be of good quality. They allow velocity distribution and variation to be consistently resolved over a large part of the E26 Lift 2 block that was not necessarily seismically active. The velocity range for the velocity models is similar to the range expected of velocity calculated directly from raw traveltimes and to velocity values reported by other authors for tomographic studies conducted in the context of block caving.

The main conclusions of this study can be summarized as follows: (1) the magnitude of velocity perturbation varies through time and appears to be strongly correlated with the intensity of microseismic activity, the mining rate, and the nature of mining activity (development versus production), (2) the velocity models may provide information allowing the inference of the cave geometry and its evolution through time, as well as the extent of the high-stress region often referred to as the seismogenic zone, (3) the observed stress distributions were not fully consistent with a widely accepted conceptual stress redistribution model, which may reflect the significant influence of rock mass inhomogeneities and the mining sequence, (4) seismicity is not necessarily confined to regions of high velocity, and (5) there was no obvious correlation in this case between geology and velocity distribution and evolution.

In summary, this paper suggests that time-lapse PST can be a key tool in understanding rock mass behavior during the development and production stages in the context of block caving and in the context of high-stress mining in general. We believe that time-lapse PST can provide important information for assessing the evolution of the caving process, thereby allowing maximization of cave performance and detection and mitigation of potential problems at an early stage.

ACKNOWLEDGMENTS

The authors would like to acknowledge numerous colleagues at Golder Associates NZ Ltd. for processing and preparing the data used in this study and A. van As and the NPM for their support, contributions, and permission to publish this work. We would also like to thank A. Ouellet, E. Tassé, J. Tod, and H. D. Neeve of Golder Associates in Montreal, whose generous contributions and constructive comments helped improve this paper. Finally, we are grateful to I. Vasconcelos, the associate editor, and P. Hanssen for their constructive reviews.

REFERENCES

- Bostock, M., and J. Van Decar, 1995, Upper mantle structure of the northern Cascadia subduction zone: Canadian Journal of Earth Sciences, **32**, 1–12, doi: [10.1139/e95-001](https://doi.org/10.1139/e95-001).
- Brady, B. H., 2004, Rock mechanics: For underground mining: Springer.
- Brown, E. T., 2007, Block caving geomechanics, 2nd ed.: Julius Kruttschnitt Mineral Research Center, JKMR Monograph Series in Mining and Mineral Processing.
- Chen, D., 1996, Geotechnical assessment of block cave mining in Northparkes Mines, NSW, Australia: Proceedings of the 2nd North American Rock Mechanics Symposium, 261.
- Christensen, N., and H. Wang, 1985, The influence of pore pressure and confining pressure on dynamic elastic properties of Berea sandstone: Geophysics, **50**, 207–213, doi: [10.1190/1.1441910](https://doi.org/10.1190/1.1441910).
- De Beer, W., J.-A. Ardito, J.-P. Mercier, J. P. Mercier, and V. Falmagne, 2012, Beyond coloured balls: Making sense of large volumes of micro seismic data with diverse source mechanisms: in Proceedings of the 6th International Seminar on Deep and High Stress Mining, The Australian Centre for Geomechanics, 149–160.
- Flores, G., 2005, Rock mass response to the transition from open pit to underground cave mining: Ph.D. thesis, University of Queensland.
- Gangi, A. F., and R. L. Carlson, 1996, An asperity-deformation model for effective pressure: Tectonophysics, **256**, 241–251, doi: [10.1016/0040-1951\(95\)00167-0](https://doi.org/10.1016/0040-1951(95)00167-0).
- Gibowicz, S. J., A. Kijko, S. Gibowicz, A. Kijko, and S. J. Gibowicz, 1994, An introduction to mining seismology: Academic Press.
- Gurevich, B., 2004, A simple derivation of the effective stress coefficient for seismic velocities in porous rocks: Geophysics, **69**, 393–397, doi: [10.1190/1.1707058](https://doi.org/10.1190/1.1707058).
- Gutenberg, B., and C. F. Richter, 1965, Seismicity of the earth and associated phenomena: Hafner.
- Hofmann, R., X. Xu, M. Batzle, M. Prasad, A. K. Furre, and A. Pillitteri, 2005, Effective pressure or what is the effect of pressure?: The Leading Edge, **24**, 1256–1260, doi: [10.1190/1.2149644](https://doi.org/10.1190/1.2149644).
- Hudyma, M., Y. Potvin, and D. Allison, 2007a, Seismic monitoring of the Northparkes Lift 2 block cave — Part 1: Undercutting: The Journal of the Southern African Institute of Mining and Metallurgy, **108**303–334.
- Hudyma, M., Y. Potvin, and D. Allison, 2007b, Seismic monitoring of the Northparkes Lift 2 block cave — Part 2: Production caving: The Journal of the Southern African Institute of Mining and Metallurgy, **108**335–354.
- Lebedev, S., 2003, Upper mantle beneath Southeast Asia from *S* velocity tomography: Journal of Geophysical Research, **108**, L2048, doi: [10.1029/2000JB000073](https://doi.org/10.1029/2000JB000073).
- Lévéque, J. J., and F. Masson, 1999, From ACH tomographic models to absolute velocity models: Geophysical Journal International, **137**, 621–629, doi: [10.1046/j.1365-246x.1999.00808.x](https://doi.org/10.1046/j.1365-246x.1999.00808.x).
- Lickfold, V., D. Cooke, S. Smith, and T. Ullrich, 2003, Endeavour copper-gold porphyry deposits, Northparkes, New South Wales: Intrusive history and fluid evolution: Economic Geology, **98**, 1607–1636, doi: [10.2113/gsecongeo.98.8.1607](https://doi.org/10.2113/gsecongeo.98.8.1607).
- Lomax, A., A. Zollo, P. Capuano, and J. Virieux, 2001, Precise, absolute earthquake location under Somma-Vesuvius volcano using a new three-dimensional velocity model: Geophysical Journal International, **146**, 313–331, doi: [10.1046/j.0956-540x.2001.01444.x](https://doi.org/10.1046/j.0956-540x.2001.01444.x).
- Lye, A., G. Crook, L. Kolff van Oosterwijk, and P. Lewis, 2006, The discovery history of the Northparkes deposits: Presented at Sydney Mineral Exploration Discussion Group (SMEDG) Mineral Exploration Geoscience in New South Wales Mines & Wines Conference.
- Maxwell, S., and R. Young, 1996, Seismic imaging of rock mass responses to excavation: Elsevier.
- Mendecki, A. J., 1996, Seismic monitoring in mines: Springer.
- Mercier, J. P., M. Bostock, J. Cassidy, K. Dueker, J. Gaherty, E. Garner, J. Revenaugh, and G. Zandt, 2009, Body-wave tomography of western Canada: Tectonophysics, **475**, 480–492, doi: [10.1016/j.tecto.2009.05.030](https://doi.org/10.1016/j.tecto.2009.05.030).
- Niu, F., P. G. Silver, T. M. Daley, X. Cheng, and E. L. Majer, 2008, Preseismic velocity changes observed from active source monitoring at the Parkfield SAFOD drill site: Nature, **454**, 204–208, doi: [10.1038/nature07111](https://doi.org/10.1038/nature07111).
- Nur, A., and J. Byerlee, 1971, An exact effective stress law for elastic deformation of rock with fluids: Journal of Geophysical Research, **76**, 6414–6419, doi: [10.1029/JB076i026p06414](https://doi.org/10.1029/JB076i026p06414).
- Prasad, M., and M. Manghnani, 1997, Effects of pore and differential pressure on compressional wave velocity and quality factor in Berea and Michigan sandstones: Geophysics, **62**, 1163–1176, doi: [10.1190/1.1444217](https://doi.org/10.1190/1.1444217).
- Rawlinson, N., and M. Sambridge, 2003, Seismic traveltime tomography of the crust and lithosphere: Advances in Geophysics, **46**, 81–198, doi: [10.1016/S0065-2687\(03\)46002-0](https://doi.org/10.1016/S0065-2687(03)46002-0).
- Sethian, J. A., 1999, Fast marching methods: SIAM Review, **41**, 199–235, doi: [10.1137/S0036144598347059](https://doi.org/10.1137/S0036144598347059).
- Silver, P. G., T. M. Daley, F. Niu, and E. L. Majer, 2007, Active source monitoring of crosswell seismic travel time for stress-induced changes: Bulletin of the Seismological Society of America, **97**, 281–293, doi: [10.1785/0120060120](https://doi.org/10.1785/0120060120).
- Sol, S., C. J. Thomson, J. M. Kendall, D. White, J. C. VanDecar, and I. Asudeh, 2002, Seismic tomographic images of the cratonic upper mantle beneath the Western Superior Province of the Canadian Shield — A remnant Archean slab?: Physics of the Earth and Planetary Interiors, **134**, 53–69, doi: [10.1016/S0031-9201\(02\)00081-X](https://doi.org/10.1016/S0031-9201(02)00081-X).
- Thurber, C. H., 1992, Hypocenter-velocity structure coupling in local earthquake tomography: Physics of the Earth and Planetary Interiors, **75**, 55–62, doi: [10.1016/0031-9201\(92\)90117-E](https://doi.org/10.1016/0031-9201(92)90117-E).
- Westman, E., 2012, Passive seismic tomography for three-dimensional time-lapse imaging of mining-induced rock mass changes: The Leading Edge, **31**, 338–345, doi: [10.1190/1.3694902](https://doi.org/10.1190/1.3694902).
- White, H., W. de Beer, H. White, A. van As, and D. Allison, 2004, Implementation of seismic monitoring systems in a block-cave environment, 559–554.
- Wyllie, M. R. J., A. R. Gregory, and G. H. F. Gardner, 1958, An experimental investigation of factors affecting elastic wave velocities in porous media: Geophysics, **23**, 459–493, doi: [10.1190/1.1438493](https://doi.org/10.1190/1.1438493).
- Yamamura, K., 2003, Long-term observation of in situ seismic velocity and attenuation: Journal of Geophysical Research, **108**, 2317–2331, doi: [10.1029/2002JB002005](https://doi.org/10.1029/2002JB002005).
- Young, R., and S. Maxwell, 1992, Seismic characterization of a highly stressed rock mass using tomographic imaging and induced seismicity: Journal of Geophysical Research, **97**, 12361–12373, doi: [10.1029/92JB00678](https://doi.org/10.1029/92JB00678).
- Zelt, C. A., and P. J. Barton, 1998, Three-dimensional seismic refraction tomography: A comparison of two methods applied to data from the Faeroe Basin: Journal of Geophysical Research, **103**, 7187–7210, doi: [10.1029/97JB03536](https://doi.org/10.1029/97JB03536).